Single-shot measurement of wavelength-resolved state of polarization dynamics in ultrafast lasers using dispersed division-of-amplitude

Qiang Wu, Lei Gao, Yulong Cao, Stefan Wabnitz, Zhenghu Chang, Ai Liu, Jingsheng Huang, Tao Zhu**

Q. Wu, L. Gao, Y. Cao, Z. Chang, A. Liu, J. Huang, T. Zhu
Key Laboratory of Optoelectronic Technology & Systems (Ministry of Education),
Chongqing University, Chongqing 400044, China
E-mail: gaolei@cqu.edu.cn, zhutao@cqu.edu.cn

S. Wabnitz
Dipartimento di Ingegneria dell'Informazione, Elettronica e Telecomunicazioni, Sapienza Università di Roma, via Eudossiana 18, 00184 Roma, Italy

S. Wabnitz
CNR-INO, Istituto Nazionale di Ottica, Via Campi Flegrei 34, 80078 Pozzuoli (NA), Italy

Keywords: mode-locking lasers, solitons, dissipative solitons, dispersive Fourier transforms, division-of-amplitudes, polarization states

The characterization of state of polarization (SOP) of ultrafast laser emission is relevant in several application fields such as field manipulation, pulse shaping, testing of sample characteristics, and biomedical imaging. Nevertheless, since high-speed detection and wavelength-resolved measurements can not be simultaneously achieved by commercial polarization analyzers, single-shot measurements of the wavelength-resolved SOP of ultrafast laser pulses has rarely been reported so far. Here, we propose a new method for single-shot, wavelength-resolved SOP measurement, which exploits the method of division-of-amplitude under the far-field transformation. A large accumulated chromatic dispersion is utilized to time-stretch the laser pulses via dispersive Fourier transform, so that spectral information is mapped into a temporal waveform. By calibrating our test matrix with different wavelengths, wavelength-resolved SOP measurements are achieved, based on the division-of-amplitude approach, combined with high speed opto-electronic processing. As a proof-of-concept demonstration, we could reveal the complex wavelength-dependent SOP dynamics in the

build-up of dissipative solitons, as well as the apparent discrepancy of SOP between dispersive sidebands and their generating solitons. Our method paves the way for single-shot measurement and intelligent control of ultrafast lasers with wavelength-resolved SOP structures, which could promote further investigations of polarization-related optical signal processing techniques, such as pulse shaping, and hyperspectral polarization imaging.

1. Introduction

Characterizing the state of polarization (SOP) of lasers plays an essential role in various fields, ranging from fundamental science to applications. At variance with single frequency lasers, ultrafast lasers have a much wider spectrum, due to mode-locking into ultrashort pulse trains. Recently, it has been found that ultrafast lasers may generate complex wavelength-dependent polarization structures.[1-10] Therefore, the precise characterization of the wavelength-resolved SOP of ultrafast lasers is of great fundamental and technological significance. For example, polarization-dependent regimes and complex polarization evolution processes, including polarization-locked [1,2] and polarization rotation phenomena,[3] have been widely reported in laser cavities combining nonlinearity with dispersion. Meanwhile, ultrafast manipulation,[11,12] pulse shaping[13,14] and biomedical imaging[15-20] require accurate measurements of the SOP of ultrafast lasers. Nevertheless, since high-speed detection and wavelength-resolved measurements can not be simultaneously achieved by commercial polarization analyzers, single-shot measurements of the wavelength-resolved SOP of ultrafast laser pulses have, to our knowledge, rarely been reported.

Well-established polarization measurement methods have been proposed for characterizing continuous wave (CW) laser emission. However, methods such as the time-sharing method or rotating wave plate [21,22] method suffer the disadvantage of low speed of operation. Although beam splitting methods, such as the division-of-amplitude method, where four components of rapidly varing signals can be simultaneously detected,[23-27] permits high-speed SOP detection, they fail to be wavelength-resolved, due to their lack of capability to perform high-speed measurement of wide spectrum data. Therefore, combining high-speed SOP detection with wavelength-resolved measurement is essential for carrying out single-shot measurements of the wavelength-resolved SOP from ultrafast lasers.

In this article, we propose and experimentally demonstrate a new method for the single-shot measurement of wavelength-resolved SOP for ultrafast lasers. Our approach is based on combining the division-of-amplitude technique with the dispersive Fourier transform (DFT) method. In previous work, temporal-spectral mapping through time-stretching DFT was

utilized for characterizing the rapidly evolving spectra from ultrafast lasers.[9,10,28-37] Here, we decompose the single-shot spectra by projecting them in a spatial optical module based on the division-of-amplitude principle. This permits us to detect the four intensity components which are necessary to obtain the SOP by means of a high-speed photodetection system. After calibrating our SOP detection system matrix by means of a CW laser with tunable wavelength, we are able to reconstruct a wavelength-resolved set of Stokes parameters. Our method is tested on two different types of ultrafast lasers. First, we identify wavelength-dependent SOP structures in a dissipative soliton (DS) laser operating in the net normal cavity dispersion regime. Second, we reveal the dynamics of the formation of Kelly sidebands during the process of an anomalous dispersion laser cavity generating conventional solitons (CS). Our method may thus lead to finding new regimes of fascinating SOP evolution dynamics in the emission of ultrafast lasers. These dynamics are otherwise hidden from us, when the SOP information is neglected in the study of ultrafast lasers.

2. Results and Discussion

2.1. Principle and Experimental Setup

The precise SOP measurement of any ultrafast laser can be achieved by obtaining their wavelength-resolved Stokes parameters with a high-speed detection system. As shown in **Figure 1**a, a single-shot spectrum measurement is performed via DFT within a section of DCF. Due to the large group velocity dispersion, ultrafast pulses propagating in a DCF undergo a far-field transformation. When negliecting higher-order dispersion terms, a linear wavelength-to-time mapping is obtained according to the relationship:[28]

$$\Delta t = |D| L \Delta\lambda \tag{1}$$

Where, Δt is the time duration after mapping, D is the group delay dispersion coefficient, L is the propagation distance, and $\Delta\lambda$ is the optical spectral bandwidth of the laser pulses.

After time-stretching, the dispersed pulses are splitted into four optical channels by the division-of-amplitude technique.[23,24] For each individual wavelength λ, its SOP is described by a wavelength-resolved Stokes vector $S(\lambda) = (S_0, S_1, S_2, S_3)^T$, which can be reconstructed at each wavele from the measured intensity vector from the four channels

$I(\lambda)=(I_0,I_1,I_2,I_3)^T$ at each wavelength. The intensity detected by the photodetector in each channel can be expressed as a linear combination of four Stokes parameters $I_i(\lambda)=a_{i1}S_0+a_{i2}S_1+a_{i3}S_2+a_{i4}S_3$. We use a 4×4 wavelength-dependent system matrix $A(\lambda)$, in order to express the relationships between the vector of intensities and the Stokes vector as $I(\lambda)=A(\lambda)S(\lambda)$. When the determinant of matrix $A(\lambda)$ is non vanishing, viz., $\det[A(\lambda)]\neq0$, the inverse of $A(\lambda)$ can be found. Then, by measuring the intensities of the four channels, the wavelength-resolved SOPs can be calculated as:

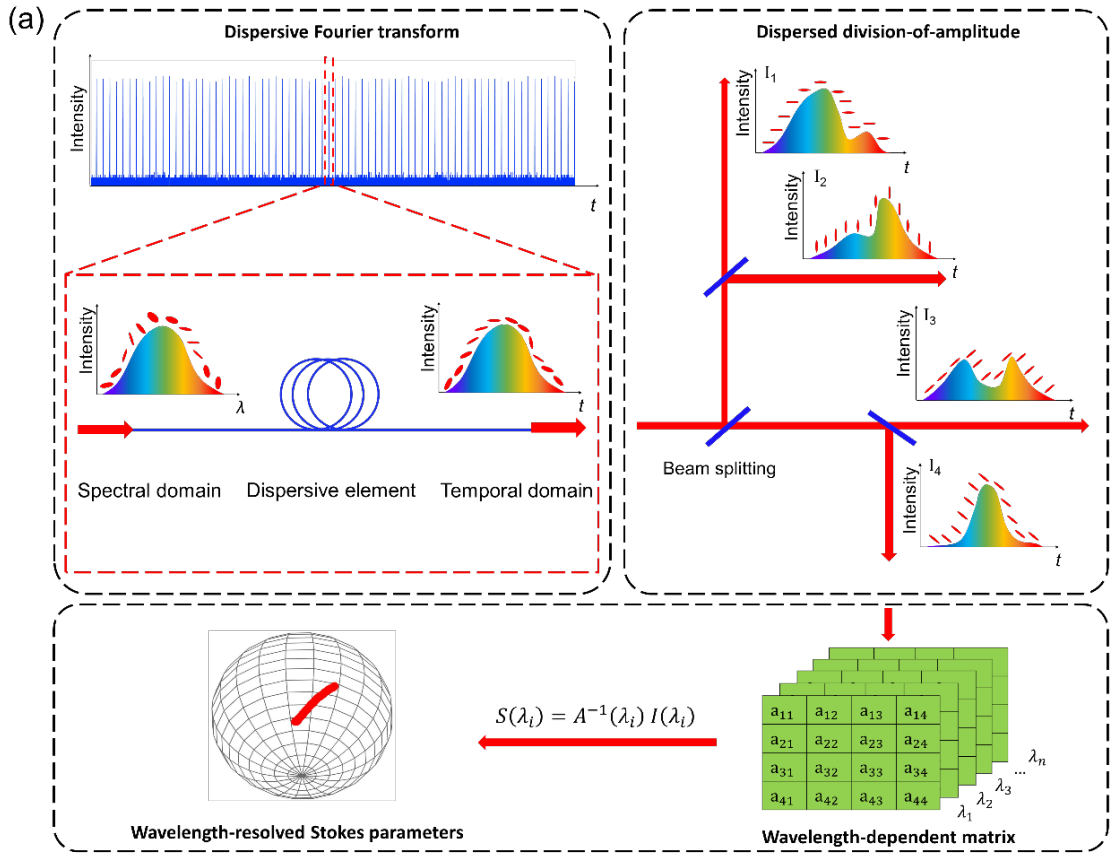

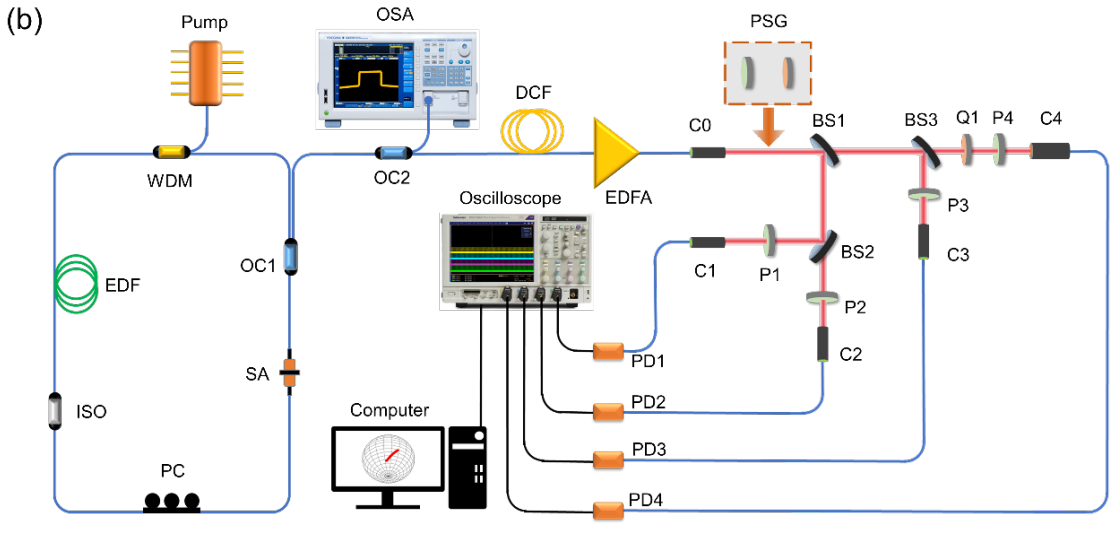

Figure 1. a) Principle of DFT and dispersed division-of-amplitude method. An ultrafast pulse is time-stretched, and the optical spectrum is mapped into the temporal domain, under the far-field approximation imparted by propagation in a dispersive medium. Next, the dispersed signal is splitted into four channels, and after calibration of each individual wavelength, a wavelength-resolved system matrix is built. b) Schematic of the fiber laser cavity and measurement system containing a 980 nm pump laser (Pump), erbium-doped fiber (EDF), wavelength division multiplexer (WDM), saturable absorber (SA), isolator (ISO), polarization controller (PC), optical coupler (OC1-OC2), dispersion compensating fiber (DCF), erbium-doped fiber amplifier (EDFA), optical spectrum analyzer (OSA), collimator (C0-C4), beam splitters (BS1-BS3), analyzers (P1-P4), quarter-wave plate (Q1), polarization state generator (PSG), photodetectors (PD1-PD4) and digital oscilloscope. The DS and CS can be generated by changing the type of gain fiber and the net dispersion of cavity. Blue lines denote laser beams propagating in fiber, and red lines indicate free-space laser propagation. Black lines are electrical signals.

$$S(\lambda) = A^{-1}(\lambda) I(\lambda) \tag{2}$$

Some additional SOP parameters can be deduced from the Stokes parameters. For example, the spherical orientation angle θ and the ellipticity angle ψ of the polarization ellipse can be calculated from the Stokes parameters, $\theta = \arctan\left(S_2/S_1\right)/2$, $\psi = \arctan\left(S_3/\sqrt{S_1^2+S_2^2}\right)/2$. Whereas SOP fluctuations can ben mesured by computing the relative distance between two points on Poincaré sphere:

$$\Delta S = \sqrt{\left(S_1^{'} - S_1\right)^2 + \left(S_2^{'} - S_2\right)^2 + \left(S_3^{'} - S_3\right)^2} \tag{3}$$

Details about the experimental setup and associated devices are given in the Experimental Section.

2.2. Calibration of the Measuring System

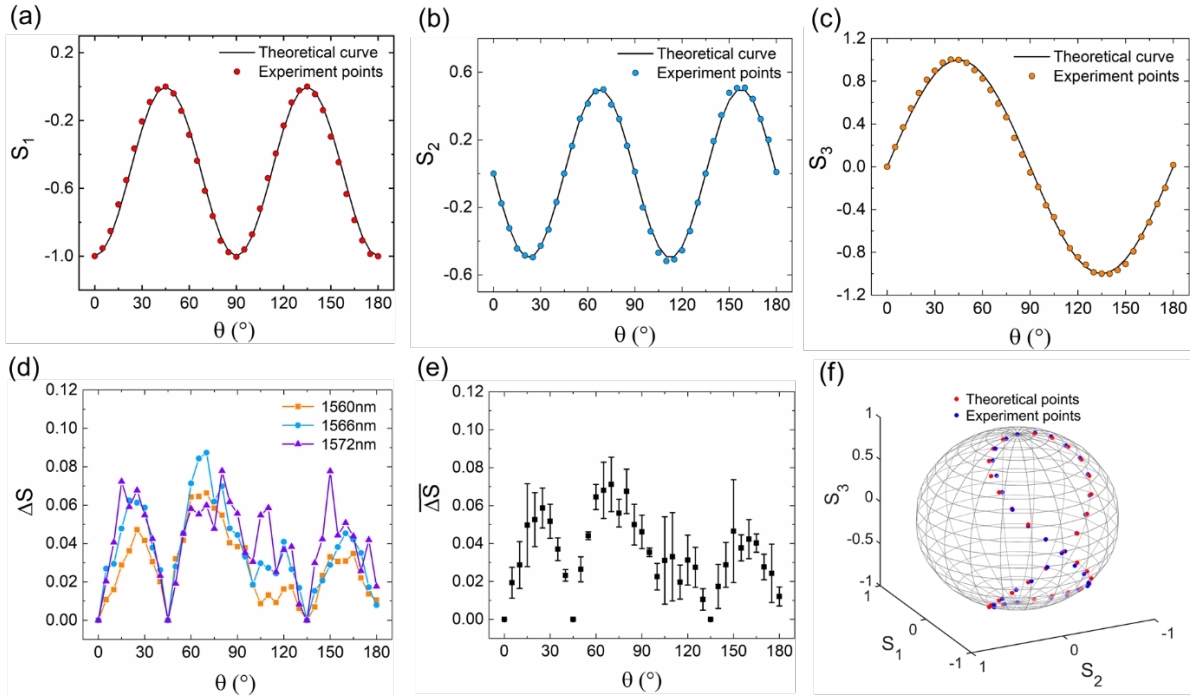

Figure 2. Calibration of division-of-amplitude. a-c) theoretical value (black solid curve) and experimental points (colored circles) of the S_1, S_2 and S_3 Stokes parameters at 1550 nm. The polarizer is set at the angle of 90°, and the rotation angle of the quarter-wave plate is 180°. As a result, the three Stokes parameters periodically evolve with the angle θ, with period of 90°, 90° and 180°, respectively. d-e) Deviation and mean error of the Stokes parameters at the wavelengths of 1560 nm, 1566 nm and 1572 nm, respectively: these values cover almost entirely the spectral bandwidth that we used. The mean deviation is less than 0.07 for all of the three wavelengths. f) Theoretical points (red circles) and measured SOPs (blue circles) on the Poincaré sphere. The trace forms a figure-of-eight pattern moving from the north pole to the south pole, as determined by the combination of the polarizer angle and the quarter-wave plate.

Before carrying out the measurements, the system of division-of-amplitude needs to be calibrated at first, so the wavelength-dependent system matrix $A(\lambda)$ can be determined. In this process, we used a tunable CW laser as the optical source, with a wavelength ranging between 1500 nm and 1630 nm. We conducted the calibration covering the entire spectral range of the signal under test, with a step of 0.5 nm. Next, we fixed the polarizer at the angle $\theta = 90°$, and we progressively rotated the quarter-wave plate from the intersection angle (see Experimental Section, division of amplitude part) of 0° up to 180°, with a step of 5°, across a span of 180°. In order to reduce the effects associated with imperfections of the optical

elements, we used the equator-poles method for calibration.[27] Four points, located on the equator and at the poles, are chosen as four known vectors.

Figure 2 depicts the calibration results of based on equator-poles method. The four vectors of SOP are $(1,-1,0,0)^T$, $(1,0,1,0)^T$, $(1,0,0,1)^T$, $(1,0,0,-1)^T$. As shown in **Figure 2**a-c, the measured S_1, S_2 and S_3 at 1550 nm overlap with the theoretical curves. A mean standard deviation of 0.03 was obtained between the positions of the measured and the theoretical Stokes vectors on the Poincaré sphere, as depicted in **Figure 2**f. After calibration at 1550 nm, we tested the division-of-amplitude system over a wide wavelength range. As displayed in **Figure 2**d-e, the selected wavelengths are 1560 nm, 1566 nm and 1572 nm. The corresponding deviations are almost the same for all of the three wavelengths. Meanwhile, the mean value of deviation for every rotation angle and for each of the three wavelengths is less than 0.07. After carrying out the calibration by means of wavelength tuning from 1555 nm to 1575 nm, we could perform accurate wavelength-resolved SOPs measurements within a range of 20 nm.

2.3. SOP Measurements of Dissipative Solitons

When optical gain is provided by a 20 m EDF with normal dispersion, we obtain the generation of a DS in the dissipative fiber laser cavity, thanks to a balance of nonlinearity, dispersion, gain, and loss.[29-31,38,39] As shown in **Figure 3**a, the averaged optical spectrum ranges from 1561 nm to

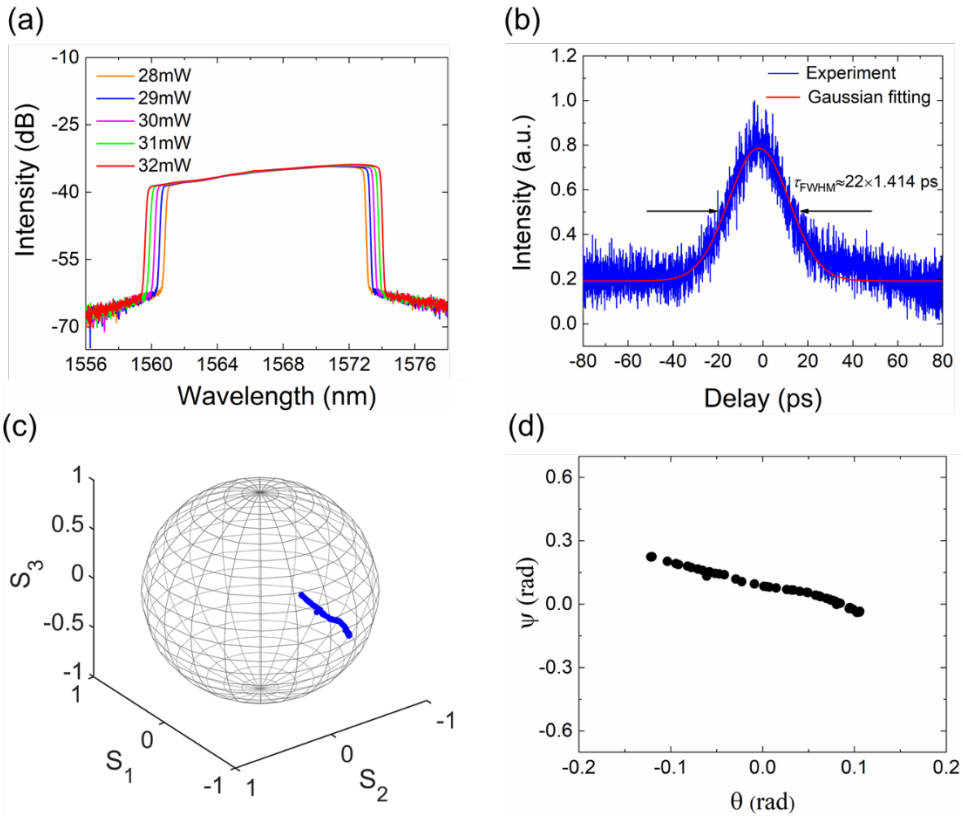

Figure 3. Characteristics of DS. a) Optical spectra for pump powers ranging from 28 mW to 32 mW. The corresponding bandwidth increases from 12 nm to 14 nm. b) Autocorrelation trace of a DS and the corresponding Gaussian fitting curve. The full width at half maximum (FWHM) of pulse duration is about 30 ps. c) SOPs measured by a commercial polarization analyzer, when the broad spectrum is filtered linearly from 1560 nm to 1574 nm by a tunable filter. d) Phase diagram based on the spherical orientation angle θ and ellipticity angle ψ calculated from the SOPs in (c). The spherical orientation angle θ variation is about 0.25 rad, and the ellipticity angle ψ variation is nearly 0.3 rad, respectively.

1573 nm at the pump power of 28 mW. As the pump power is further increased, the wave-breaking-free rectangular shaped DS spectrum is gradually broadened. The DS autocorrelation trace is fitted by a Gaussian function, shown in **Figure 3**b, and the FWHM pulse duration is of about 30 ps. Furthermore, as depicted in **Figure 3**c, we filtered the broad spectrum by a tunable optical filter (Santec, OTF-320) with bandwidth of 0.2 nm: the corresponding SOPs along all of the filtered wavelengths were measured by means of a polarization state analyzer (General Photonics, PSGA-101-A). As can be seen in **Figure 3**c, a nonlinear trajectory was obtained for the wavelength evolution of the SOP on Poincaré sphere. The corresponding phase plane trajectory, based on the spherical orientation angle θ

and ellipticity angle ψ, is illustrated in **Figure 3**d. The spherical orientation angle variation is of about 0.25 rad, and the ellipticity angle variation is equal to nearly 0.3 rad, respectively. Variation of SOP is attributed to nonlinear phase shift accumulation. Yet, these averaged measurements based on wavelength filtering are not accurate enough to reveal the details of the polarization dynamics of the generated DS.

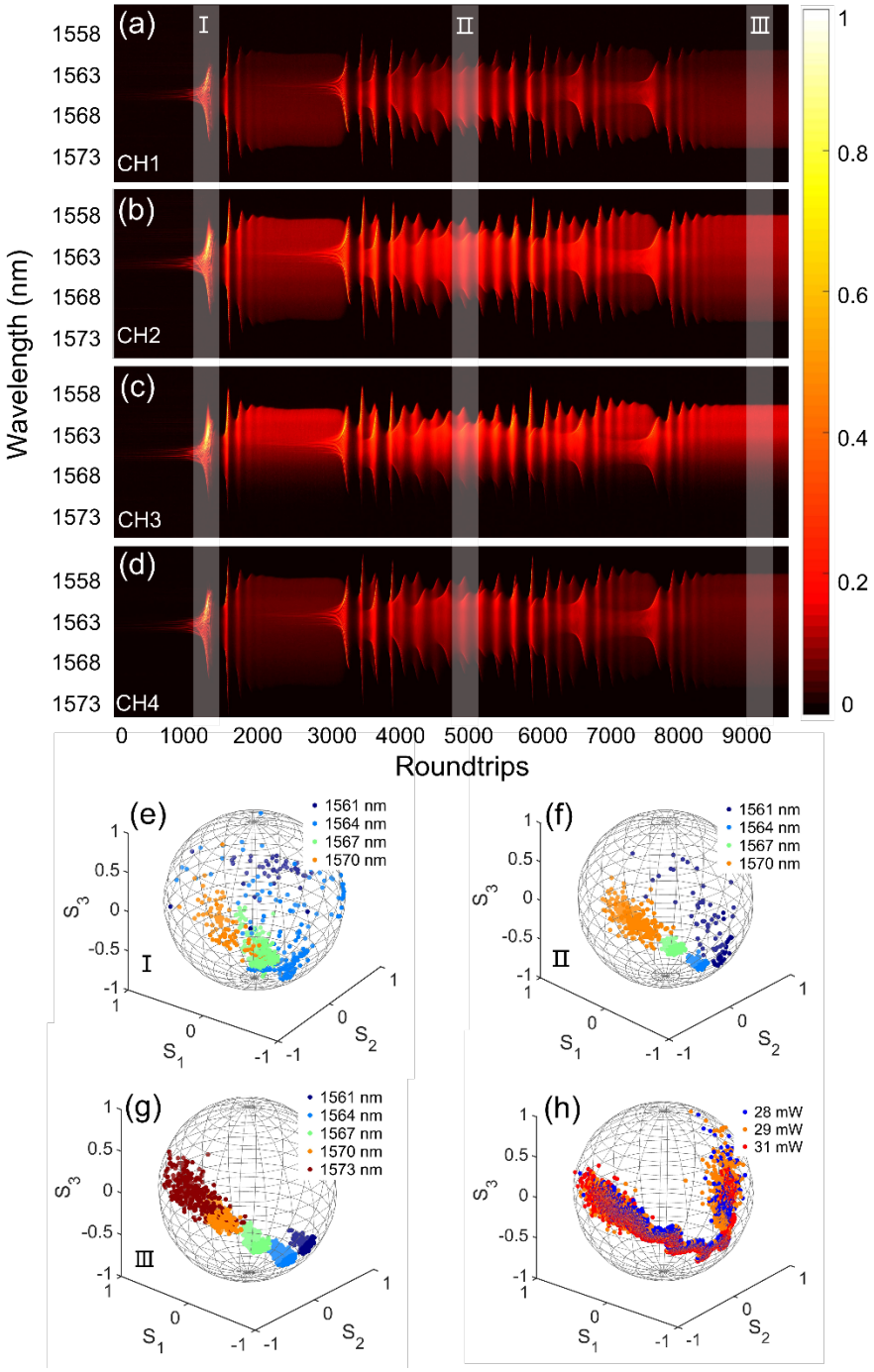

Figure 4. a-d) Single-shot spectra of four channels (CH1-CH4) associated with the DS, when the pump power is 28 mW. The three regions I, II, and III in the build-up process correspond

to spectrum broadening, spectrum oscillation and stable mode-locking and are marked by semitransparent white stripes. The associated number of roundtrips are 1100^{th}-1400^{th}, 4800^{th}-5100^{th}, 9000^{th}-9300^{th}, respectively. e-g) Reconstructed wavelength-resolved SOPs for three selected regions of DSs. SOPs evolve from a random distribution towards concentrated and ordered island. h) Reconstructed wavelength-resolved SOPs in region III for pump powers of 28 mW, 29 mW and 31 mW, respectively.

In order to unveil these dynamics, we performed single-shot wavelength-resolved transient SOPs measurements during the build-up phase of the DS, when the pump power is switched on from zero up to 28 mW. The single-shot spectra detected within the four channels are shown in **Figure 4**a-d. There are more than 9000 roundtrips with a temporal period of 134 ns. Here, the spectral information of the DS is time-stretched into 7.2 ns via DFT. In our detection system, any slight difference of arrival times within the four channels can be compensated by precisely tuning the optical paths. Based on the detected spectral intensities in the four channels, and the inverse matrix of the division-of-amplitude system, we managed to reconstruct the wavelength-resolved evolution of the normalized Stokes parameters. Specifically, in **Figure 4**a-d three regions, region I, II and III, are selected: each of them shows a distinct dynamics. For region I, spectral broadening is initiated via self-phase modulation, and it is followed by spectral intensity fluctuations. As shown in **Figure 4**e, the corresponding SOPs distribution is randomly distributed on the Poincaré sphere, in particular for wavelengths at the spectrum edges. Within region II, the broadened spectrum oscillates periodically: in **Figure 4**f, the corresponding SOP distribution appears to occupy specific regions on the Poincaré sphere. Whenever stable DSs are formed, such as in region III, then the stable mode-locking mechanism appears to dominate the SOP evolution process. As depicted in **Figure 4**g, the SOPs are distributed within island-shaped regions. These single-shot results are consistent with the observations reported in **Figure 3**c and **3**d, both indicating that a wavelength-dependent SOP distribution exists for DSs.[4,5,9] The physical mechanism behind the observed SOP dynamics can be associated with the large nonlinear frequency chirp of DSs, which eventually leads to a variation of the SOP for its different spectral components.[38,39] By increasing the pump power, the nonlinear chirp grows larger. This can be revealed by comparing the wavelength-resolved SOPs of stable DSs for different pump powers. As shown in **Figure 4**h, the SOP trajectories for three values of the pump power are similar in the middle of the spectrum, both exhibiting zig-zag-shaped fluctuations. Whereas

for wavelengths at the spectrum edges, intense SOPs fluctuations occur, whose detailed behavior cannot be quantitatively resolved.

In order to quantitatively compare the differences in SOP evolutions within different roundtrips, in **Figure 5** we report the measured Stokes parameters. For wavelength around 1561 nm in regions I and II, the Stokes parameters experience intense fluctuations, since they are associated with the newly generated frequencies which grow in the process of spectrum broadening (**Figure 5**a and b). Whereas for region III, associated with stable mode-locking, the Stokes parameters appear to be stabilized (**Figure 5**c). It should be pointed out that measuring Stokes parameters with zero values does not mean that the light depolarized. This is because in our data processing, we removed the Stokes parameter points whenever the intensities of the four channels was at the low level of the electronic noise.

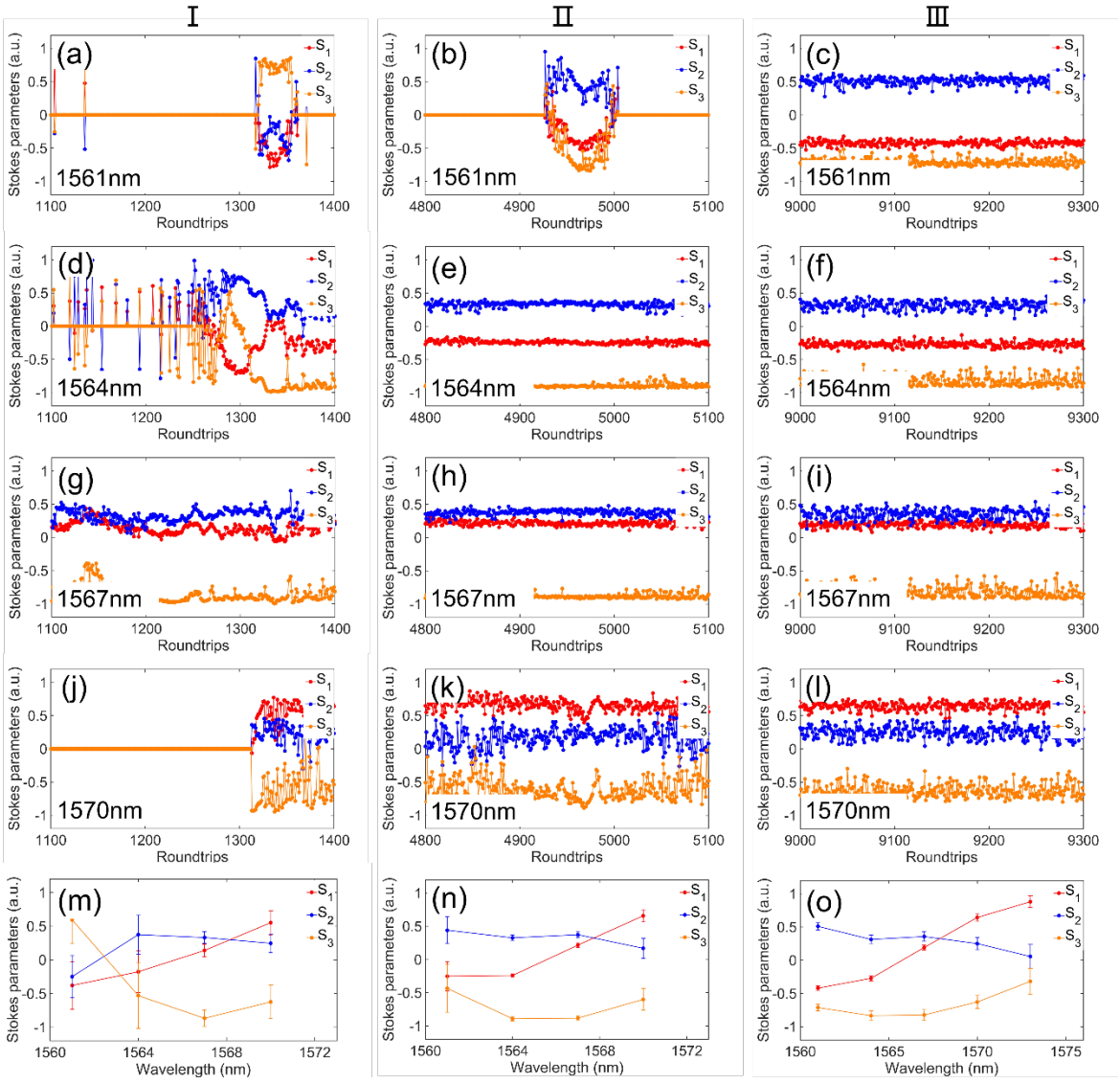

Figure 5. a-l) Stokes parameters evolution vs. number of roundtrips, for wavelengths at 1561 nm, 1564 nm, 1567 nm and 1570 nm, respectively, in the three regions I, II and III of **Figure**

4. m-o) Mean value and standard deviation of the Stokes parameters for the four selected wavelengths in these three regions.

For the wavelengths of 1564 nm and 1570 nm in region I (**Figure 5**d and j), intense oscillations and polarization conversion is observed in the process of spectral broadening. Whereas, the corresponding Stokes parameters remain stable in regions II and III. For the wavelength at 1567 nm, namely near the central part of the spectrum, the Stokes parameters always vary slightly, which suggests that SOPs within the central part of the spectrum are less affected by the process of DS build-up. Besides, as depicted in **Figure 5**m-o, we computed the mean values and standard deviations of the Stokes parameters at the four selected wavelengths as a function of the number of roundtrips in region I, II and III, respectively. As can be seen, the SOPs of wavelengths located at the spectrum edges fluctuate more intensely than SOPSs for the central portion of the spectrum, which is consistent with the previously discussed behavior. The observed large fluctuations do not originate from measurement system errors, but from the unique SOP dynamics of the DSs. The validity of such conclusion will be proved in the next section, by a comparison with the SOP dynamics of anomalous dispersion solitons.

2.4. SOP Measurements of Solitons

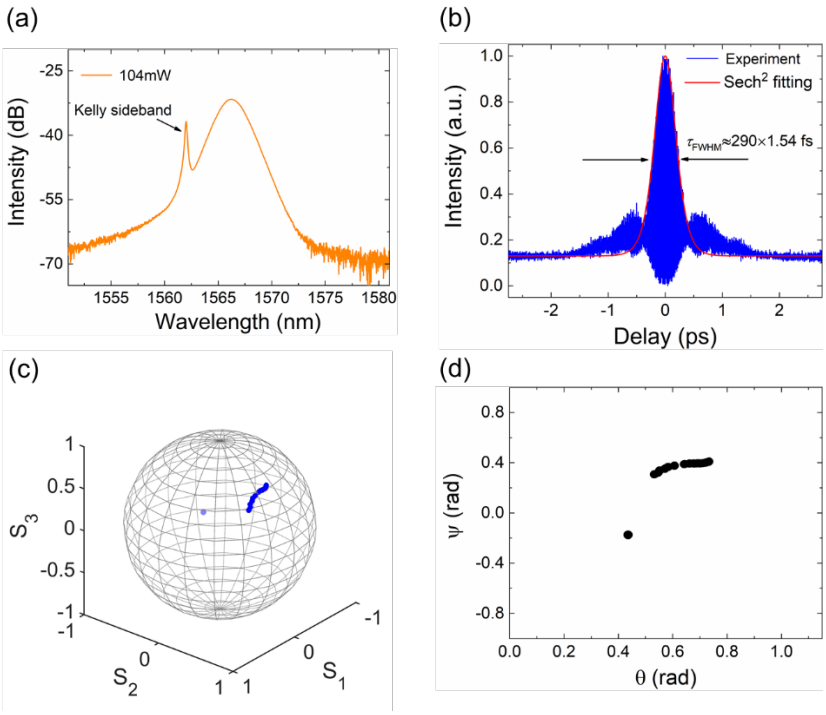

Figure 6. Characteristics of the CS fiber laser. a) Averaged optical spectrum with a single Kelly sideband for a pump power of 104 mW. The FWHM bandwidth is of about 4 nm. b) Autocorrelation trace fitted by a $sech^2$ curve: the FWHM of the CS is of about 450 fs. c) SOPs measured for the filtered wavelengths of the main peak and for the Kelly sideband. The SOP of the main CS peak is displayed as a line. The SOP of the Kelly sideband is represented by a point, located far away from the SOP of the main CS peak. d) Phase plane diagram based on the spherical orientation angle θ and ellipticity angle ψ, calculated from the SOPs in (c)**.** The net variation of the angle is less than 0.2 rad.

By replacing the gain fiber with 1 m of EDF exhibiting anomalous dispersion, we observed the generation of nonlinear Schrödinger (or conventional) solitons (CSs) in the fiber laser cavity. Here soliton formation can be understood as representing the balance of nonlinearity with anomalous dispersion, so that transform-limited pulses are formed without any phase chirping.[40,41] As shown in **Figure 6**a, the optical spectrum contains a main peak centered at 1566 nm, and a giant Kelly sideband at 1561.5 nm; here the pump power is 104 mW. In **Figure 6**b, the autocorrelation trace is measured, and fitted by a square of hyperbolic secant function, which leads to a pulse FWHM of about 450 fs. Similarly, as depicted in **Figure 6**c and d, we filtered the soliton wavelength components via a tunable optical filter, and measured the SOPs of the main soliton spectral peak as well as of the Kelly sideband by the polarization state analyzer. For the main peak, the SOPs are slowly evolving across all wavelengths. The spherical orientation angle θ varies within 0.2 rad, and the net variation of the ellipticity angle ψ is of about 0.1 rad. However, the SOP of the Kelly sideband is found to be located far away from the SOP of the main peak.

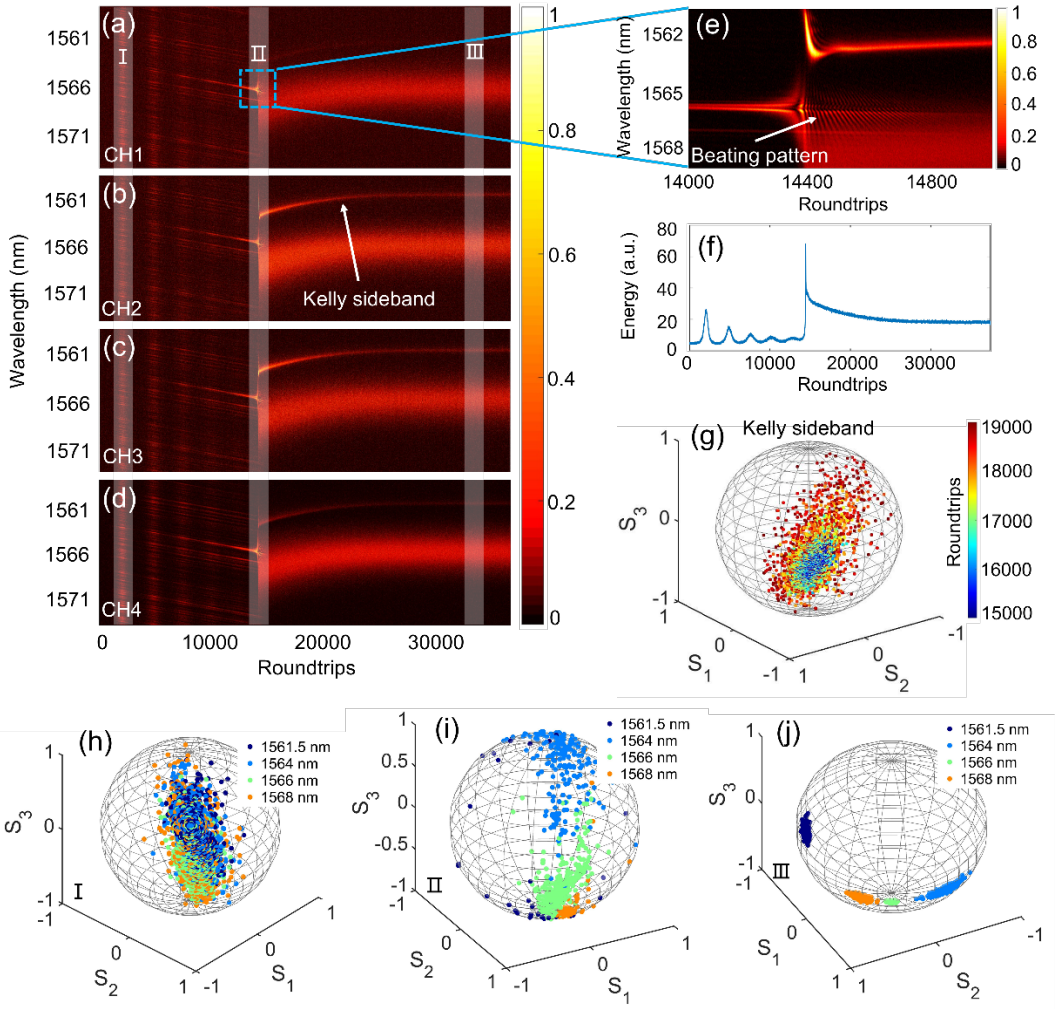

Figure 7. a-d) Single-shot spectra of the CS build-up process at four channels for a pump power of 104 mW, and over 34000 roundtrips. The three regions, marked as I, II and III (identified by white semitransparent stripes) in the CS buildup process correspond to relaxation oscillations, beating dynamics and stable mode-locking pulses. e) Beating pattern of multiple pulses in region II (blue box), occuring at about 14400th roundtrips and accompanied by the presence of a Kelly sideband. f) Integral energy calculated from (a). The energy oscillations and the giant peak correspond to the region I and II, respectively. g) Evolution trajectory of the SOP of the Kelly sideband from the 15000th roundtrip up to the 19000th roundtrip. During energy transfer from the CS, the intensity of the Kelly sideband varies and its SOP significantly changes. h-j) SOPs for the three regions I-III of CSs, corresponding to the white stripes in (a)-(d): these are colored by different wavelengths for each region.

By using our SOP detection system, we could investigate the single-shot wavelength-resolved SOPs dynamics during the build-up of solitons. The single-shot spectra within the

four channels are detected via DFT, and are shown in **Figure 7**a-d. More than 30000 roundtrips are displayed here. Three regions, named as I, II and III, are selected within the whole CS build-up process. For region I, relaxation oscillations start, and are followed by several spikes before a transition to region II: the spikes can be identified via the energy oscillations which appear in the integral energy of **Figure 7**f. We may also notice the presence of a giant peak, corresponding to region II, where mode-locking dominates. We observe a beating behavior due to the interference between the main pulse and other sub-pulses originating by wave breaking (**Figure 7**e).[36] The presence of a Kelly sideband is also identified, originating from the quasi-phase-matched generation of a dispersive wave that accompanies the periodic amplification of solitons[42-44] In **Figure 7**g, the evolution trajectory of the SOP of the Kelly sideband is reported for a number of roundtrips ranging from the 15000^{th} up to the 19000^{th}. During those roundtrips, the intensity of the Kelly sideband varies before a stable mode-locking regime is reached, and its SOP exhibits intense fluctuations. Moreover, due to the wavelength-dependent variation of the group velocity of intracavity pulses, a spectral evolution with a tilted center wavelength results in **Figure 7**a-d**.** Chromatic dispersion modifies the round-trip time, which should be properly taken into account in data processing.[45] When stable solitons are formed, region III with an uniform energy distribution is reached.

The reconstructed wavelength-resolved SOPs for the three regions I-III are shown in **Figure 7**h-j. As it is shown in **Figure 7**h, the SOP distribution for the selected wavelengths shows the presence of a random scattering around the same central SOP value. This means that, during relaxation oscillations, the different wavelength components exhibit similar phases. The accumulated nonlinear phase is not strong enough for balancing chromatic dispersion. However, whenever the gain is high enough, as shown in region II, new frequencies are generated by four-wave mixing, whenever the corresponding phase-matching condition is satisfied. Therefore, the intracavity spectrum is broadened, solitons are formed while dispersive pulses are suppressed. The soliton SOPs cover a wider area on the Poincaré sphere, as shown in **Figure 7**i. Whereas after a certain SOP smoothing period, such as for roundtrips between15000^{th} to 30000^{th}, the SOPs for all wavelengths tend to be concentrated in a small area on the Poincaré sphere, as can be seen in **Figure 7**j. For region III, stable CSs propagate in the laser cavity, and their SOP distribution on the Poincaré sphere is similar to that provided by the commercial polarimeter measurement results in **Figure 6**c. In addition, we may notice that the SOPs for the wavelength at 1561.5 nm, which corresponds to the Kelly sideband, are located far away from the SOP distribution of the main CS peak. The reason for

that can be ascribed to the previously mentioned mechanism of Kelly sideband formation.[42-44] Both solitons and dispersive waves that circulate in the fiber laser cavity experience periodic amplification, but their relative phase varies because only solitons are affected by a nonlinear phase shift. Despite the fact that the relative phase is an integer multiple of 2π at some frequencies, the SOPs of the Kelly sideband remain well distinct from the CS SOP distribution.

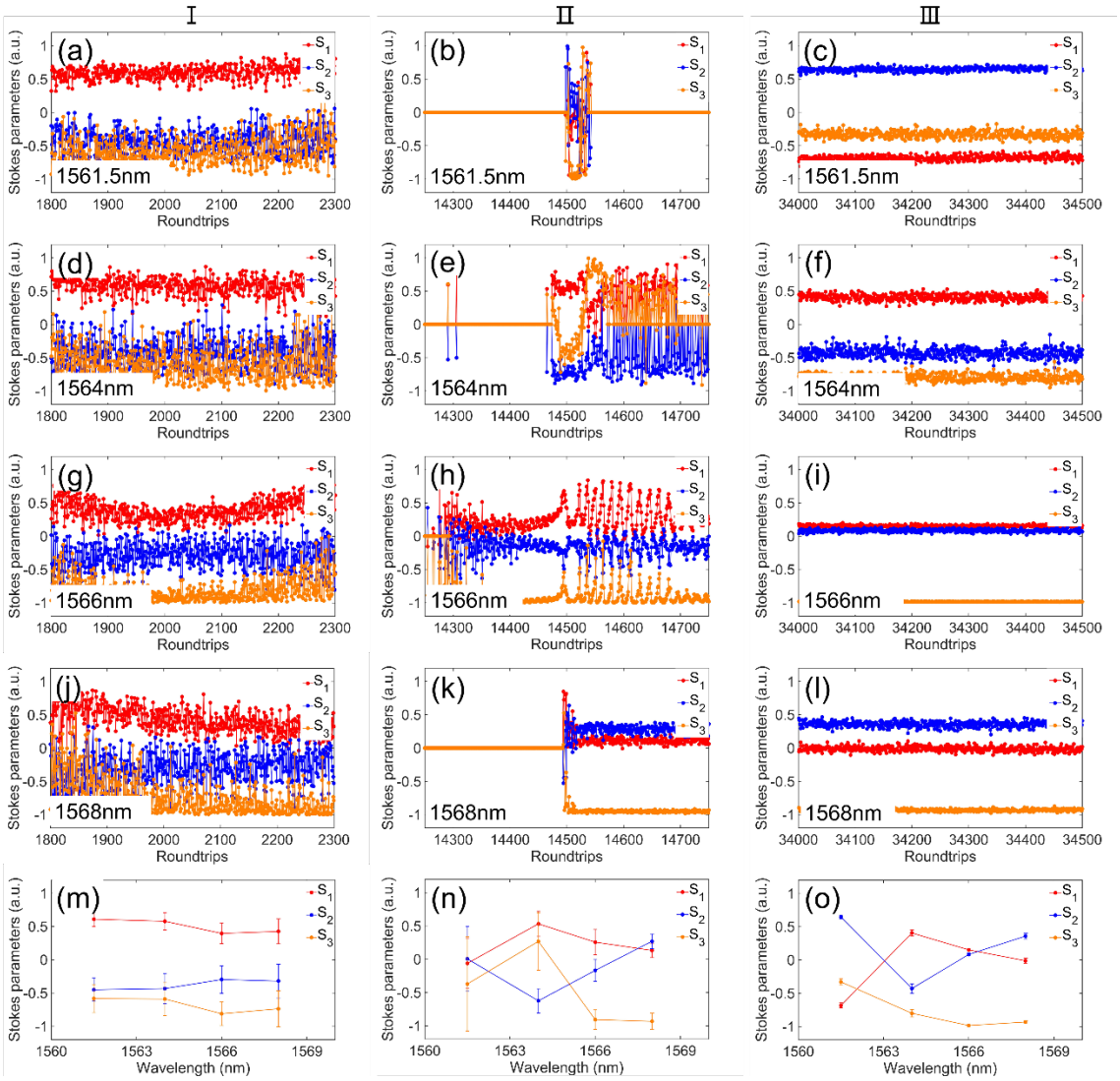

Figure 8. a-l) Stokes parameters of CSs evolving within the three regions I-III for wavelengths at 1561.5 nm, 1564 nm, 1566 nm and 1568 nm, respectively. m-o) Mean values and standard deviations of the Stokes parameters for different wavelengths in each of the three regions.

The corresponding Stokes parameters of CSs located within each of the three regions I-III are shown in **Figure 8**. For region I, due to the relaxation oscillations, the Stokes parameters experience local fluctuations and are even sliding along successive roundtrips for 1566 nm

(see **Figure 8**g) and 1568 nm (see **Figure 8**j). The associated SOP deviations are relatively high (see **Figure 8**m). In region II, for the spectral components at the edge of the spectrum, namely for 1561.5 nm and 1568 nm, the SOPs vary abruptly, owing to spectral broadening. For example, the Stokes parameters at the 1561.5 nm wavelength vanish, because of the sudden spectral shifting during the formation of CS, as shown by the single-shot spectra in **Figure 7**e. For wavelengths at 1564 nm and 1566 nm, quasi-periodic-oscillations result into the beating behavior of **Figure 7**e, whose period depends on the phase-matching interference conditions between pulses with varying temporal delays.[36] In region II, SOP fluctuations are different from those observed region I, owing to energy coupling of different spectral components (**Figure 8**n). For region III associated with stable mode-locking, the Stokes parameters are stabilized and exhibit relatively low fluctuations (**Figure 8**o).

2.5. Discussion

In our measurement system, several key parameters can be optimized, including the detection bandwidth, spectral resolution, and detecting precision. Primarily, since both the DFT and the division-of-amplitude module do not impose a main limitation, the detection bandwidth of the measurement system is essentially determined by the optoelectronic components, including the bandwidth of the photodetector, the sampling rate of the digital oscilloscope or other electronic digitizers, and possibly the data processing speed, whenever a real-time measurement is desired. Besides, the spectral resolution is also determined by the net dispersion in the DFT, in addition to the optoelectronics bandwidth. In our system, a spectral resolution of 0.2 nm is obtained. Yet, this can be further reduced down to 0.08 nm by using 2 km of DCF and 20 GHz photodectors. Of course, the nonlinearity of wavelength-to-time mapping, and the repetition rate of ultrafast lasers will limit the optimization of the available spectral resolution.

Finally, the detecting uncertainty, which can be partially revealed by the observed large SOP fluctuations, originates from the fact that we are measuring the wavelength-resolved SOPs of an ultrafast laser, rather than the SOPs of a single-frequency CW laser. When a parallel decomposition associated with a Mueller matrix is performed, as it occurs in the division-of-amplitude method, the measurement process averages all elements of the Mueller matrix via a convolution process, and the instrument response function is determined by the various instrument uncertainties, such as the measurement time (which is determined by the bandwidth of our optoelectronics components), and the spectral resolution.[46,47] For

commercial polarization analyzers used with CW lasers a low measurement speed, the photocurrents detected by the photodetectors are integrated over a relatively long measurement time and a wide spectral bandwidth. Therefore, the obtained SOPs in **Figure 3**c and **6**c appear to be more stable and localized. Whereas in our case, the measurement time is much shorter, and the spectroscopy conducted through DFT further reduces the detected photocurrents, leading to larger uncertainties. Yet, our measured SOP fluctuations for the above two types of lasers exhibit rather different properties. This indicates that these fluctuations do not originate from uncertainties of the detection system, but rather from intrisinc polarization properties of each ultrafast laser. For example, the observed wavelength-resolved SOP structure in DSs can be ascribed to the significant nonlinear phase shift which is accumulated at the lasing frequencies. Those frequencies are generated within different roundtrips, where the balance between dispersion, gain, loss, and nonlinearity may be evolving. As a result of the slowly evolving phases, the observed SOPs vary along both temporal and spectral coordinates.

3. Conclusion

In conclusion, we demonstrated a new wavelength-resolved, high-speed SOP measurement system. As a proof-of-concept demonstration, we tested and compared two different types of ultrafast lasers. When the single-shot spectra measurement by DFT is extended via the division-of-amplitude method, a new high-speed, wavelength resolved SOP measurement technique is proposed, based on reconstructing the Mueller matrix via parallel decomposition. Based on our method, experimentally investigated the nonlinear evolution dynamics in the process of the build-up of DSs and CSs. We believe that our SOP measurement method will find applications in basic research, such as ultrafast lasers measurements and studies of nonlinear optical process, and will also expand the capabilities of different polarization-related techniques, such as pulse shaping and hyperspectral polarization imaging.

4. Experimental Section

Experimental Setup: As schematically depicted in **Figure 1**b, the two ultrafast lasers share similar configuration. The DS ring cavity contains 20 m of erbium-doped fiber (EDF) with a dispersion of -12.2 ps nm^{-1} km^{-1}, forward pumped by a 976 nm diode laser through a 1550/980 nm wavelength division multiplexer (WDM). The saturable absorber (SA) is made from single-wall carbon nanotubes. The rest of the cavity includes an isolator (ISO), a

polarization controller (PC), 6.8 m of single-mode fiber with the dispersion of 18 ps nm^{-1} km^{-1}, and an optical coupler (OC1) with a 10% output port. The net normal dispersion is 0.155 ps^2. For solitons, the cavity is replaced with a 1 m EDF whose dispersion is 15.7 ps nm^{-1} km^{-1}, and 5.8 m of single-mode fiber. The net dispersion of the soliton cavity is about -0.153 ps^2.

Dispersive Fourier transform: The dispersive Fourier transform (DFT) is achieved by using 2 km of dispersion compensating fiber (DCF) with the dispersion of about -300 ps nm^{-1} km^{-1}. The temporal signal is fed into a high-speed photodetector with 8 GHz bandwidth. Moreover, taking into account the analog bandwidth of 20 GHz and the maximum sampling rate of 50 GSa s^{-1} of the digital oscilloscope (Tektronix, DSA 72004B), the electronic response is mainly limited by photodetector. According to the relationship of wavelength-to-time mapping, the spectral resolution is about 0.2 nm for our experimental setup. After the DFT, we use an erbium-doped fiber amplifier (EDFA, Amonics AEDFA-23-B-FA) to amplify the loss introduced by the DCF and various other components. The optical spectrum of the output signal is measured by an optical spectrum analyzer (OSA, Yokogawa AQ6370).

Division-of-amplitude: For the division-of-amplitude, we built the spatial system through a collimator (C0) leading to a parallel beam, which then is divided into four paths by three beam splitters (BS1-BS3) with transmission reflection ratio of 5:5. The angles of four analyzers (P1-P4) are set to 0°, 45°, 90°, and 135°, respectively, and the intersection angle between the quarter-wave plate (Q1) and analyzer in the fourth path is 45°. The orientation of 0° is parallel to the platform. In this way, any SOP, including linear polarizations and circular polarizations, can be recognized. In order to input an arbitrary SOP in the calibration process, a polarizer and a quarter-wave plate play the role of polarization state generator, which is shown on the pink plate and marked by a pink arrow. The outputs from the four channels are received by four collimators (C1-C4). Photoelectric conversion is achieved by four identical high-speed photodetectors (PD1-PD4) with a bandwidth of 8 GHz and a digital oscilloscope with a bandwidth of 20 GHz.

Supporting Information

Supporting Information is available from the Wiley Online Library or from the author.

Acknowledgements

The authors acknowledge supports from the Natural Science Foundation of China (62075021), Project supported by graduate research and innovation foundation of Chongqing, China (CYB20061), National Science Fund for Distinguished Young Scholars (61825501),

the European Research Council (ERC) under the European Union's Horizon 2020 research and innovation program (740355).

Received: ((will be filled in by the editorial staff))
Revised: ((will be filled in by the editorial staff))
Published online: ((will be filled in by the editorial staff))

References

[1] D. Y. Tang, H. Zhang, L. M. Zhao, X. Wu, *Phys. Rev. Lett.* **2008**, *101*, 153904.

[2] C. Mou, S. Sergeyev, A. Rozhin, S. Turistyn, *Opt. Lett.* **2011**, *36*, 3831.

[3] M. Liu, A. P. Luo, Z. C. Luo, W. C. Xu, *Opt. Lett.* **2017**, *42*, 330.

[4] H. Zhang, D. Tang, L. Zhao, Q. Bao, K. P. Loh, *Opt. Commun.* **2010**, *283*, 3334.

[5] K. Krupa, K. Nithyanandan, P. Grelu, *Optica* **2017**, *4*, 1239.

[6] Y. Luo, J. Cheng, B. Liu, Q. Sun, L. Li, S. Fu, D. Liu, *Sci. Rep.* **2017**, *7*, 1.

[7] Y. Song, Z. Liang, H. Zhang, Q. Zhang, L. Zhao, D. Shen, D. Tang, *IEEE Photon. J.* **2017**, *9*, 1.

[8] F. Lu, Q. Lin, W. H. Knox, G. P. Agrawal, *Phys. Rev. Lett.* **2004**, *93*, 183901.

[9] L. Gao, Y. Cao, S. Wabnitz, H. Ran, L. Kong, Y. Li, T. Zhu, *Photon. Res.* **2019**, *7*, 1331.

[10] L. Gao, L. Kong, Y. Cao, S. Wabnitz, H. Ran, Y. Li, T. Zhu, *Opt. Express* **2019**, *27*, 23830.

[11] Y. Yang, K. Kelley, E. Sachet, S. Campione, T. S. Luk, J. P. Maria, I. Brener, *Nat. Photonics* **2017**, *11*, 390.

[12] Z. Zhang, Y. Chen, S. Cui, F. He, M. Chen, Z. Zhang, J. Zhang, *Nat. Photonics* **2018**, *12*, 554.

[13] T. Brixner, G. Gerber, *Opt. Lett.* **2001**, *26*, 557.

[14] F. Fraggelakis, E. Stratakis, P. A. Loukakos, *Appl. Surf. Sci.* **2018**, *444*, 154.

[15] T. Novikova, A. Pierangelo, A. De Martino, A. Benali, P. Validire, *Opt. Photonics News* **2012**, *23*, 26.

[16] N. Ghosh, A. I. Vitkin, *J. Biomed. Opt.* **2011**, *16*, 110801.

[17] S. L. Jacques, *Phys. Med. Biol.* **2013**, *58*, R37.

[18] Y. Zhao, L. Zhang, Q. Pan, *Appl. Opt.* **2009**, *48*, D236.

[19] H. He, M. Sun, N. Zeng, E. Du, S. Liu, Y. Guo, H. Ma, *J. Biomed. Opt.* **2014**, *19*, 106007.

[20] M. Garcia, C. Edmiston, R. Marinov, A. Vail, V. Gruev, *Optica* **2017**, *4*, 1263.

[21] T. Kihara, *Appl. Mech. Mater.* **2005**, *3*, 235.

[22] B. Schaefer, E. Collett, R. Smyth, D. Barrett, B. Fraher, *Am. J. Phys.* **2007**, *75*, 163.

[23] R. M. A. Azzam, *Opt. Acta* **1982**, *29*, 685.

[24] R. M. A. Azzam, *Opt. Acta* **1985**, *32*, 1407.

[25] A. M. El-Saba, R. M. A. Azzam, M. A. G. Abushagur, *Opt. lett.* **1996**, *21*, 1709.

[26] S. Krishnan, S. Hampton, J. Rix, B. Taylor, R. M. A. Azzam, *Appl. Opt.* **2003**, *42*, 1216.

[27] S. Krishnan, *J. Opt. Soc. Am. A* **1992**, *9*, 1615.

[28] K. Goda, B. Jalali, *Nat. Photonics* **2013**, *7*, 102.

[29] P. Ryczkowski, M. Närhi, C. Billet, J. M. Merolla, G. Genty, J. M. Dudley, *Nat. Photonics* **2018**, *12*, 221.

[30] J. Peng, M. Sorokina, S. Sugavanam, N. Tarasov, D. V. Churkin, S. K. Turitsyn, H. Zeng, *Commun. Phys.* **2018**, *1*, 1.

[31] H. J. Chen, M. Liu, J. Yao, S. Hu, J. B. He, A. P. Luo, Z. C. Luo, *Opt. Express* **2018**, *26*, 2972.

[32] C. Lapre, C. Billet, F. Meng, G. Genty, J. M. Dudley, *OSA Continuum* **2020**, *3*, 275.

[33] X. Wang, J. He, H. Shi, B. Mao, M. Feng, Z. Wang, Y. G. Liu, *Opt. Lett.* **2020**, *45*, 4782.

[34] J. Peng, H. Zeng, *Phys. Rev. Appl.* **2019**, *12*, 034052.

[35] K. Krupa, K. Nithyanandan, U. Andral, P. Tchofo-Dinda, P. Grelu, *Phys. Rev. Lett.* **2017**, *118*, 243901.

[36] X. Liu, D. Popa, N. Akhmediev, *Phys. Rev. Lett.* **2019**, *123*, 093901.

[37] X. Liu, X. Yao, Y. Cui, *Phys. Rev. Lett.* **2018**, *121*, 023905.

[38] P. Grelu, N. Akhmediev, *Nat. Photonics* **2012**, *6*, 84.

[39] D. Mao, X. M. Liu, L. R. Wang, X. H. Hu, H. Lu, *Laser Phys. Lett.* **2010**, *8*, 134.

[40] A. F. Runge, D. D. Hudson, K. K. Tam, C. M. de Sterke, A. Blanco-Redondo, *Nat. Photonics* **2020**, *14*, 492.

[41] L. Yun, *Opt. Express* **2017**, *25*, 18751.

[42] S. M. J. Kelly, *Electron. Lett.* **1992**, *28*, 806.

[43] R. Weill, A. Bekker, V. Smulakovsky, B. Fischer, O. Gat, *Phys. Rev. A* **2011**, *83*, 043831.

[44] X. Hu, J. Guo, J. Ma, S. W. Yoo, D. Y. Tang, *Laser Phys. Lett.* **2020**, *17*, 095103.

[45] X. Wei, B. Li, Y. Yu, C. Zhang, K. K. Tsia, K. K. Wong, *Opt. Express* **2017**, *25*, 29098.

[46] K. Hingerl, R. Ossikovski, *Opt. Lett.* **2016**, *41*, 219.

[47] M. Miranda-Medina, E. Garcia-Caurel, A. Peinado, M. Stchakovsky, K. Hingerl, R. Ossikovski, *Appl. Surf. Sci.* **2017**, *421*, 656.